Inorg. Chem. **2004**, *43*, 6383–6396

Synthesis, Characterization, and Photochemical and Computational Investigations of Ru(II) Heterocyclic Complexes Containing 2,6-dimethylphenylisocyanide (CNx) Ligand

John M. Villegas,[†] Stanislav R. Stoyanov,[†] Wei Huang,[†] Loranelle L. Lockyear,[‡] Joseph H. Reibenspies,[§] and D. Paul Rillema*[,†]

Department of Chemistry, Wichita State University, 1845 North Fairmount Street, Wichita, Kansas 67260-0051, Department of Chemistry, Bethany College, 421 North First Street, Lindsborg, Kansas 67456-1897, and Department of Chemistry, Texas A&M University, P.O. Box 30012, College Station, Texas 77842-3012

Received July 8, 2004

The isocyanide ligand forms complexes with ruthenium(II) bis-bipyridine of the type $[Ru(bpy)_2(CNx)Cl](CF_3SO_3)$ (**1**), $[Ru(bpy)_2(CNx)(py)](PF_6)_2$ (**2**), and $[Ru(bpy)_2(CNx)_2](PF_6)_2$ (**3**) (bpy = 2,2′-bipyridine, py = pyridine, and CNx = 2,6-dimethylphenylisocyanide). The redox potentials shift positively as the number of CNx ligands increases. The metal-to-ligand charge-transfer (MLCT) bands of the complexes are located at higher energy than 450 nm and blue shift in proportion to the number of CNx ligands. The complexes are not emissive at room temperature but exhibit intense structured emission bands at 77 K with emission lifetimes as high as 25 μs. Geometry optimization of the complexes in the singlet ground and lowest-lying triplet states performed using density functional theory (DFT) provides information about the orbital heritage and correlates with X-ray and electrochemical results. The lowest-lying triplet-state energies correlate well with the 77 K emission energies for the three complexes. Singlet excited states calculated in ethanol using time-dependent density functional theory (TDDFT) and the conductor-like polarizable continuum model (CPCM) provide information that correlates favorably with the experimental absorption spectra in ethanol.

Introduction

Studies of complexes containing 2,6-dimethylphenylisocyanide as a ligand have received attention from investigators because isocyanide ligands are known to act like carbon monoxide by serving as s donors and/or p acceptors.[1−7] In fact, some evidence indicates that isocyanide (CNx) is a much better s donor than CO.[2] Because of its versatility in accommodating a wide range of electronic and structural environments, the ligand has been used to study complexes containing low-valent transition metals (V, Nb, Ta)[3] as well as metals with relatively high oxidation states (Cr, Mn, Mo).[2,4−6]

Because isocyanide ligands are expected to provide a strong ligand field,[8] the metal-centered (d−d) states are expected to remain at high energies and might not be readily accessible for radiationless deactivation of excited metal-to-ligand charge-transfer (MLCT) or charge-transfer (CT) states. Consequently, complexes containing these ligands could provide potentially useful excited-state properties for solar

* To whom correspondence should be addressed. E-mail: paul.rillema@wichita.edu.
[†] Wichita State University.
[‡] Bethany College.
[§] Texas A&M University.

(1) (a) Malatesta, L.; Bonati, F. *Isocyanide Complexes of Metals*; Wiley: New York, 1969. (b) Bonati, F.; Minghetti, G. *Inorg. Chim. Acta* **1974**, *9*, 95.
(2) Stacy, N. E.; Conner, K. A.; McMillin, D. R.; Walton, R. A. *Inorg. Chem.* **1986**, *25*, 3649.
(3) (a) Barybin, M. V.; Young, V. G.; Ellis, J. E. *J. Am. Chem. Soc.* **1998**, *120*, 429. (b) Barybin, M. V.; Young, V. G.; Ellis, J. E. *J. Am. Chem. Soc.* **1999**, *121*, 9237.
(4) (a) Mialki, W. S.; Wigley, D. E.; Wood, T. E.; Walton, R. A. *Inorg. Chem.* **1982**, *21*, 480. (b) Bohling, D. A.; Mann, K. R. *Inorg. Chem.* **1983**, *22*, 1561.
(5) (a) Nielson, R. M.; Wherland, S. *Inorg. Chem.* **1985**, *24*, 1803. (b) Brant, P.; Cotton, F. A.; Sekutowski, J. C.; Wood, T. E.; Walton, R. A. *J. Am. Chem. Soc.* **1979**, *101*, 6588.
(6) Szalda, D. J.; Dewan, J. C.; Lippard, S. J. *Inorg. Chem.* **1981**, *20*, 3851.
(7) (a) Shi, Q. Z.; Richmond, T. G.; Trogler, W. C.; Basolo, F. *Inorg. Chem.* **1984**, *23*, 957. (b) Richter-Addo, G. B.; Legzdins, P. *Metal Nitrosyls*; Oxford University Press: New York, 1992.
(8) Sarapu, A. C.; Fenske, R. F. *Inorg. Chem.* **1975,** *14*, 247.

10.1021/ic049099r CCC: $27.50
Published on Web 09/08/2004

cell and medicinal dyes. An important aspect to consider in any attempt to study new excited states based on ruthenium(II) polypyridyl complexes is a detailed understanding of how chemical changes influence the excited-state photophysical and photochemical processes.[9] The properties include (a) excited-state lifetimes determined by the rates of radiative (k_r) and nonradiative (k_{nr}) processes and by the rates for population and subsequent decay of the low-lying d−d states, (b) photochemical instability dictated by the availability of low-lying d−d states and their inherent reactivity,[10] and (c) ground-state and excited-state redox potentials.[11] To date, there is very little information available on isocyanide complexes of Ru(II)-containing heterocyclic ligands that are well-known for exhibiting excited-state emission and electron-transfer behavior.[12,13] Here, we extend these reports to include a series of ruthenium(II) diimine dyes containing isocyanide ligands that show very interesting electronic and photophysical properties, and we also include computational studies on their properties.

Computational studies based on density functional theory (DFT) have proven to be important in the interpretation of experimental spectroscopic and electrochemical results. Earlier work in our laboratory[14] has revealed a linear relationship between the energies of the highest occupied molecular orbitals (HOMOs) and lowest unoccupied molecular orbitals (LUMOs) of a series of ruthenium(II) heterocycles and the redox potentials of the complexes. As another example, the spatial distribution of the frontier orbitals for a ferrocene−C60−dinitrobenzene triad correlated very well with the cyclic voltammetry results.[15] It was also possible to account for vibrational spectra by DFT calculations for rhodium isocyanide complexes[16] and trinuclear ruthenium isocyanide clusters.[17]

The calculated molar absorptivities (ϵ) based on singlet excited-state oscillator strengths in the gas phase using the time-dependent density functional theory (TDDFT) method have been reported to correlate with the experimental values of ϵ determined in solution, but calculations in the gas phase by the TDDFT method do not always give the right energies for optical transitions in solution.[18a−c] However, including solvent effects in the calculations through the conductor-like polarizable continuum model (CPCM) method leads to better optical energies, but overestimates the value of ϵ.[18d] For interpretation of singlet and triplet excited-state properties of transition metal complexes in solution, the tandem use of TDDFT and polarizable continuum model (PCM) calculations has produced dramatic changes in positions of optical transitions and assignments of the excited states for Pt(II) and W(V) double salts,[19] as well as ruthenium(II) and osmium(II) polypyridyl complexes,[20] and is the primary method used in our report.

Experimental Section

Materials. The ligand 2,4-dimethylphenylisocyanide was purchased from Fluka. Optima-grade methanol and NH_4OH were purchased from Fisher Scientific, and acetonitrile, NH_4PF_6, $AgCF_3SO_3$, and 2,2′-bipyridine (bpy) were purchased from Sigma-Aldrich. AAPER Alcohol and Chemical Company was the source of absolute ethanol. $RuCl_3 \cdot 3H_2O$ was obtained from Pressure Chemical Company. *cis*-$[Ru(bpy)_2Cl_2]$ was prepared by refluxing a mixture of $RuCl_3 \cdot 3H_2O$, bpy, and LiCl in DMF overnight.[21] A 4:1 (v/v) mixture of ethanol and methanol was used to prepare solutions for emission spectral and emission lifetime studies. Elemental analyses were performed by Desert Analytics Laboratory, Tucson, AZ.

Instrumentation and Physical Measurements. UV/vis spectra were obtained using a Hewlett-Packard model 8452A diode array spectrophotometer. IR spectra were acquired using a Nicolet Avatar 360 FT-IR spectrophotometer. Proton NMR spectra were obtained using a Varian Inova 400 FT-NMR spectrometer. ESI-MS spectra were collected using a Finnigan LCQ-Deca ion trap mass spectrometer (Thermoquest, San Jose, CA). An EG&G PAR model 263A potentiostat/galvanostat was used to obtain the cyclic voltammograms. The measurements were carried out in a typical H-cell using a platinum disk working electrode, a platinum wire counter electrode, and a Ag/AgCl reference electrode in acetonitrile. The supporting electrolyte used was 0.1 M tetrabutylammonium hexafluorophosphate (TBAH). Ferrocene was added as the electrochemical reference. Corrected emission spectra were collected using a Spex Tau3 fluorometer. The excited-state lifetimes were determined using an OPOTEK optical parametric oscillator pumped by a frequency-tripled Continuum Surlite Nd:YAG laser. Excited-state emission lifetimes were collected as previously explained.[22] The Origin 6.1 program by OriginLab Corporation was used for the curve-fitting analysis.

X-ray Crystallography Data Collection. A Bausch and Lomb 10× microscope was used to identify a suitable colorless plate 0.2 mm × 0.2 mm × 0.1 mm from a representative sample of crystals of $[Ru(bpy)_2(CNx)_2](PF_6)_2$ grown by slow evaporation of ethanol. The crystal was coated in a cryogenic protectant (paratone) and was then fixed to a loop, which, in turn, was fashioned to a copper mounting pin. The mounted crystal was then placed in a cold nitrogen stream (Oxford) maintained at 110 K.

(9) Caspar, J. V.; Meyer, T. J. *Inorg. Chem.* **1983**, *22*, 2444.
(10) (a) Durham, B.; Caspar, J. V.; Nagle, J. K.; Meyer, T. J. *J. Am. Chem. Soc*. **1982**, *104*, 4803. (b) Van Houten, J.; Watts, R. J. *Inorg. Chem*. **1978**, *17*, 3381. (c) Wallace, W. M.; Hoggard, P. E. *Inorg. Chem.* **1980**, *19*, 2141. (d) Porter, G. B.; Sparks, R. H. *J. Photochem*. **1980**, *13*, 123.
(11) Bock, C. R.; Connor, J. A.; Gutierrez, A. R.; Meyer, T. J.; Whitten, D. G.; Sullivan, B. P.; Nagle, J. K. *J. Am. Chem. Soc.* **1979**, *101*, 4815.
(12) Seddon, E. A.; Seddon, K. *The Chemistry of Ruthenium*; Elsevier: Amsterdam, 1984; Chapter 15.
(13) Connor, J. A.; Meyer, T. J.; Sullivan, B. P. *Inorg. Chem*. **1979**, *18*, 1388.
(14) Stoyanov, S. R.; Villegas, J. M.; Rillema, D. P. *Inorg. Chem*. **2002**, *41*, 2941.
(15) D'Souza, F.; Zandler, M. E.; Smith, P. M.; Deviprasad, G. R.; Klykov, A.; Fujitsuka, M.; Ito, O. *J. Phys. Chem. A* **2002**, *106*, 649.
(16) Moigno, D.; Callejas-Gaspar, B.; Gil-Rubio, J.; Werner, H.; Kiefer, W. *J. Organomet. Chem.* **2002**, *661*, 181.
(17) Zavarine, I. S.; Kubiak, C. P.; Yamaguchi, T.; Ota, K.; Matsui, T.; Ito, T. *Inorg. Chem*. **2000**, *39*, 2696.
(18) (a) Monat, J. E.; Rodriguez, J. H.; McCusker, J. K. *J. Phys. Chem. A* **2002**, *106*, 7399. (b) Rodrigues, J. H.; Wheeler, D. E.; McCusker, J. K. *J. Am. Chem. Soc.* **1998**, *120*, 12051. (c) Stoyanov, S. R.; Villegas, J. M.; Rillema, D. P. *Inorg. Chem*. **2003**, *42*, 7852. (d) Stoyanov, S. R.; Villegas, J. M.; Rillema, D. P. *Inorg. Chem. Commun.* **2004**, *7*, 838.
(19) Barone, V.; Fabrizi de Biani, F.; Riuz, E.; Sieklucka, B. *J. Am. Chem. Soc.* **2001**, *123*, 10742.
(20) Guillemoles, J.-F.; Barone, V.; Joubert, L.; Adamo, C. *J. Phys. Chem. A* **2002**, *106*, 11345.
(21) Sullivan, B. P.; Salmon, D. J.; Meyer, T. J. *Inorg. Chem*. **1978**, *17*, 3334.
(22) Villegas, J. M.; Stoyanov, S. R.; Rillema, D. P. *Inorg. Chem*. **2002**, *41*, 6688.

Table 1. Crystal Data for $[Ru(bpy)_2(CNx)_2](PF_6)_2$, **3**

formula	$C_{38}H_{34}F_{12}N_6P_2Ru$
formula weight	965.72
crystal size, mm	0.20 × 0.20 × 0.10
crystal system	triclinic
space group	$P\bar{1}$
a, Å	22.747(4)
b, Å	8.9247(15)
c, Å	20.813(3)
α, deg	89.974(3)
β, deg	109.997(2)
γ, deg	89.691(3)
V, Å^3	3970.3(11)
Z	4
density (calculated), g cm^{-1}	1.615
absorption coefficient, mm^{-1}	0.570
F(000)	1944
θ range for data collection, deg	1.15−25.00
index ranges	$-25 \le h \le 27$, $-10 \le k \le 10$, $-24 \le l \le 24$
reflections collected	32648
independent reflections	13835 [*R*(int) = 0.0707]
completeness to *θ* = 25.00°	98.9%
maximum and minimum transmission	0.9452 and 0.8946
goodness of fit on F2	1.176
final *R* indices [$I > 2\sigma(I)$]	R1 = 0.0675, wR2 = 0.1448
R indices (all data)	R1 = 0.0995, wR2 = 0.1565
largest difference peak and hole, e Å^{-3}	1.773 and −0.639

A Bruker SMART 1000 X-ray three-circle diffractometer was employed for crystal screening, unit cell determination, and data collection. The goniometer was controlled using the SMART software suite, version 5.056 (Microsoft NT operating system). The sample was optically centered with the aid of a video camera such that no translations were observed as the crystal was rotated through all positions. The detector was set at 5.0 cm from the crystal sample (CCD-PXL-KAF2, SMART 1000, 512 × 512 pixel). The X-ray radiation employed was generated from a Mo sealed X-ray tube (K_a = 0.70173 Å with a potential of 50 kV and a current of 40 mA) and filtered with a graphite monochromator in parallel mode (175-mm collimator with 0.5-mm pinholes).

Dark currents were obtained for the appropriate exposure time of 30 s, and a rotation exposure was taken to determine crystal quality and the X-ray beam intersection with the detector. The beam intersection coordinates were compared to the configured coordinates, and changes were made accordingly. The rotation exposure indicated acceptable crystal quality, and the unit cell determination was undertaken. Sixty data frames were taken at widths of 0.3° with an exposure time of 10 s. More than 200 reflections were centered, and their positions were determined. These reflections were used in the autoindexing procedure to determine the unit cell. A suitable cell was found and refined by nonlinear least-squares and Bravais lattice procedures and is reported here in Table 1. The unit cell was verified by examination of the *hkl* overlays on several frames of data, including zone photographs. No supercell or erroneous reflections were observed.

After careful examination of the unit cell, a standard data collection procedure was initiated. This procedure consists of collection of one hemisphere of data using *ω* scans, involving the collection 1201 0.3° frames at fixed angles for *φ*, 2*θ*, and *χ* (2*θ* = −28°, *χ* = 54.73°) while varying *ω*. Each frame was exposed for 30 s and contrasted against a 30-s dark-current exposure. The complete data collection was performed for a duration of approximately 13 h at 110 K. No significant intensity fluctuations of equivalent reflections were observed.

After data collection, the crystal was measured carefully for size, morphology, and color. These measurements are reported in Table 1.

Preparation of Compounds

(1) $[Ru(bpy)_2(CNx)Cl](CF_3SO_3)$. A 0.33-g (0.63-mmol) sample of $Ru(bpy)_2Cl_2 \cdot 2H_2O$ was mixed with 0.31 g (2.36 mmol) of 2,6-dimethylphenylisocyanide in a 100-mL round-bottomed flask. The mixture was dissolved in 50 mL of methanol and was refluxed for 5−8 h. Ten milliliters of a saturated solution of $AgCF_3SO_3$ in water was added. The solution was heated for 30 min and was filtered to remove AgCl. The filtrate was evaporated in vacuo until about 5 mL of the solution was left in the flask. The solution was slowly added to 100 mL of ether. The reddish-orange precipitate that formed was filtered and dried in a vacuum. Yield: 0.37 g (95%). MS: *m*/*z* = 580 amu for $[Ru(bpy)_2(CNx)Cl]^+$. Anal. Calcd for $RuC_{30}H_{25}N_5ClF_3SO_3$ (%): C, 49.42; H, 3.46; N, 9.61. Found: C, 50.63; H, 3.87; N, 10.26. ^{1}H NMR (DMSO): *δ* ppm 2.09 (s, 6H), 7.15 (t, 3H, *J* = 2.7 Hz), 7.38 (dd, 1H, *J* = 1.2, 6.6 Hz), 7.52 (dd, 1H, *J* = 0.9, 6.8 Hz), 7.63 (dd, 1H, *J* = 0.9, 5.6 Hz), 7.82 (dd, 2H, *J* = 0.9, 7.5 Hz), 7.95 (dd, 1H, *J* = 1.2, 6.3 Hz), 8.05 (dd, 1H, *J* = 1.5, 8.0 Hz), 8.17 (dd, 1H, *J* = 1.5, 7.8 Hz), 8.25 (dd, 1H, *J* = 1.5, 8.1 Hz), 8.37 (dd, 1H, *J* = 1.5, 7.8 Hz), 8.69 (d, 1H, *J* = 7.8 Hz), 8.79 (t, 3H, *J* = 9.0 Hz), 9.48 (dd, 1H, *J* = 0.9, 5.6 Hz), 9.65 (dd, 1H, *J* = 0.9, 5.4 Hz).

(2) $[Ru(bpy)_2(CNx)(py)](PF_6)_2$. A 0.36-g (0.50-mmol) sample of **1** was dissolved in 30 mL of ethanol, and the solution was added to 0.26 g (1.0 mmol) of $AgCF_3SO_3$ in a 100-mL round-bottomed flask. The mixture was refluxed for 2 h and was filtered to remove AgCl. One milliliter of a saturated solution of $AgCF_3SO_3$ in pyridine was added to the filtrate, which was then refluxed for another 4 h. The solvent was evaporated in vacuo until about 5−10 mL of the solution was left in the flask. Then, 10 mL of a saturated solution of NH_4PF_6 in water was added. A yellow precipitate formed, which was filtered and dried in vacuo. The solid was dissolved in acetone, filtered, and reprecipitated in water. Yield: 0.40 g (87%). MS: *m*/*z* = 769 amu for $[Ru(bpy)_2(CNx)(py)](PF_6)^+$. Anal. Calcd for $RuC_{34}H_{30}N_6P_2F_{12}$ (%): C, 44.70; H, 3.31; N, 9.20. Found: C, 44.58; H, 3.50; N, 9.22. ^{1}H NMR (DMSO): *δ* ppm 2.08 (s, 6 H), 7.17 (t, 3H, *J* = 3.0 Hz), 7.47 (dd, 3H, *J* = 1.2, 6.6 Hz), 7.65 (dd, 1H, *J* = 0.9, 7.2 Hz), 7.75 (dd, 1H, *J* = 0.9, 6.0 Hz), 7.93 (m, 4H), 8.13 (dd, 1H, *J* = 1.5, 7.5 Hz), 8.25 (dd, 1H, *J* = 1.5, 7.8 Hz), 8.30 (dd, 1H, *J* = 1.5, 7.2 Hz), 8.43 (dd, 2H, *J* = 0.9, 8.1 Hz), 8.59 (dd, 2H, *J* = 0.9, 8.1 Hz), 8.75 (dd, 3H, *J* = 1.2, 8.1 Hz), 8.89 (dd, 1H, *J* = 0.9, 8.1 Hz), 9.62 (dd, 1H, *J* = 0.9 Hz, 4.5 Hz).

(3) $[Ru(bpy)_2(CNx)_2](PF_6)_2$. A 0.33-g (0.63-mmol) sample of $Ru(bpy)_2Cl_2 \cdot 2H_2O$ was dissolved in 50 mL of ethanol, and the solution was added to 0.33 g (1.28 mmol) of $AgCF_3SO_3$ in a 100-mL round-bottomed flask. The solution was refluxed for 3 h and then allowed to cool to room temperature, after which it was filtered to remove AgCl. To the dark-red-colored filtrate, a 0.22-g (1.68-mmol) portion of 2,6-dimethylphenylisocyanide was added. The solution was refluxed overnight. Then, 2 mL of a saturated solution of $AgCF_3SO_3$ in concentrated NH_4OH was added, and the solution was refluxed for another 1−2 h. After the solution

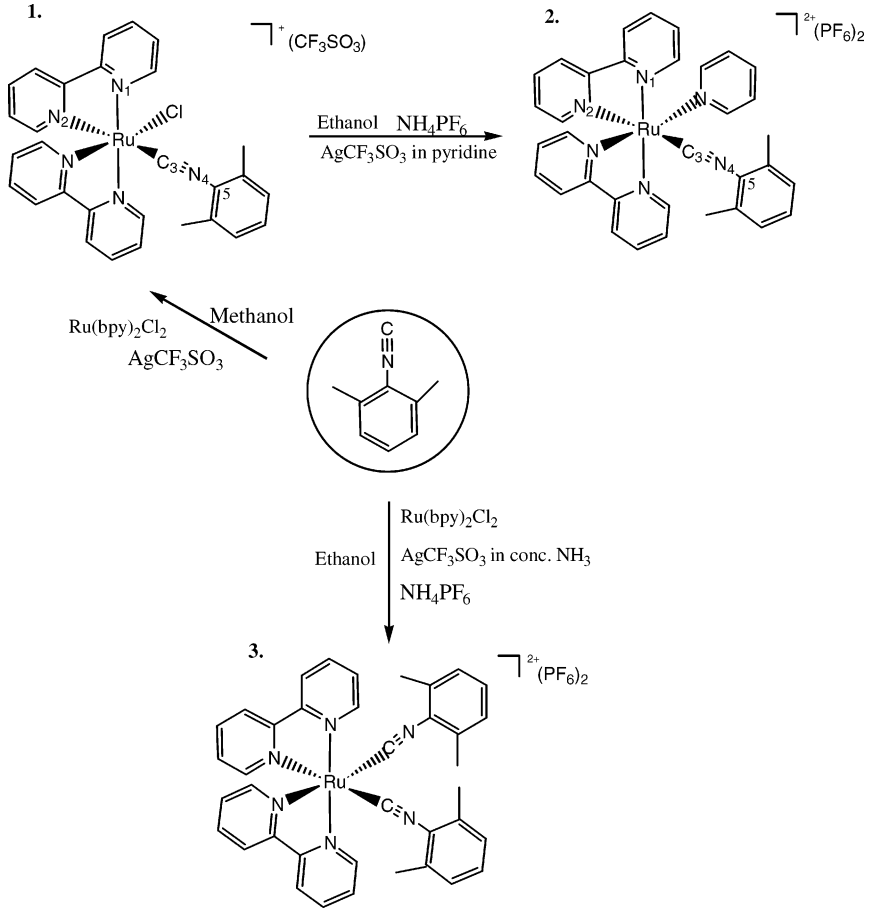

Figure 1. Schematic diagram of the synthesis of the complexes.

had been allowed to cool, 5 mL of a saturated solution of NH_4PF_6 in water was added. A yellowish-brown precipitate formed, which was filtered and dried in vacuo. Yield: 0.47 g (90%). MS: $m/z = 821$ amu for $[Ru(bpy)_2(CNx)_2](PF_6)^+$. Anal. Calcd for $RuC_{38}H_{34}N_6P_2F_{12}$ (%): C, 47.26; H, 3.55; N, 8.70. Found: C, 47.17; H, 3.80; N, 8.71.^{1}H NMR (DMSO): δ ppm 2.08 (s, 12 H), 7.22 (m, 6H), 7.63 (dd, 2H, $J = 1.5$, 6.9 Hz), 7.74 (dd, 2H, $J = 0.9$, 4.8 Hz), 7.95 (dd, 2H, $J = 1.5$, 6.0 Hz), 8.31 (dd, 2H, $J = 1.5$, 7.8 Hz), 8.47 (dd, 2H, $J = 1.2$, 7.5 Hz), 8.85 (dd, 2H, $J = 0.9$, 8.4 Hz), 8.92 (dd, 2H, $J = 0.9$, 8.4 Hz), 9.37 (dd, 2H, $J = 0.9$, 5.1 Hz).

Results

Synthesis. Complexes **1**−**3** were prepared according to the scheme presented in Figure 1. The ligand CNx was refluxed with $Ru(bpy)_2Cl_2$ overnight in methanol, and then a saturated solution of $AgCF_3SO_3$ in water was added. Complex **1** was recovered upon solvent evaporation. Similarly, **1** was also made from a precursor complex, $[Ru(bpy)_2(CF_3SO_3)Cl]$, that was prepared by first reacting $AgCF_3SO_3$ with $Ru(bpy)_2Cl_2$ in ethanol. The CNx ligand was then added to $[Ru(bpy)_2(CF_3SO_3)Cl]$ to form **1**; a red-orange solid was recovered upon evaporation of the solvent. Complex **2** was prepared by reacting **1** in ethanol with $AgCF_3SO_3$ in pyridine. This was followed by the addition of NH_4PF_6 to yield a yellow precipitate of the desired product.

Finally, **3** was prepared by reacting $Ru(bpy)_2Cl_2$ with $AgCF_3SO_3$ in ethanol and then adding excess CNx ligand in the presence of a saturated solution of $AgCF_3SO_3$ in NH_4OH. Upon addition of NH_4PF_6, a yellowish-brown precipitate was formed. The synthesized complexes were characterized by mass, IR, and ^{1}H NMR spectroscopies and elemental analysis.

X-ray Crystal Structure Determination of 3. Figure 2 shows the structure of **3** determined by X-ray crystallography.[23] Selected bond distances and angles of **3** are listed in Table 2. Complex **3** adopted a distorted octahedral geometry. The angles of the trans ligands at the metal center were 176.0(3)° for C(30)−Ru(1)−N(3), 174.4(3)° for C(21)−Ru(1)−N(2), and 166.5(2)° for N(1)−Ru(1)−N(4). The Ru−N(diimine) bond lengths of the complex were found to be longer than the Ru−C(CNx) bond lengths. The Ru−N bond lengths trans to the CNx ligands were considerably longer, by ∼0.03−0.04 Å, compared to the Ru−N distances cis to the ligands. These results are not surprising considering the

(23) The structure was solved and refined in the triclinic space group $P\bar{1}$. As suggested by the unit cell dimensions, alternative lattice symmetry (monoclinic) can be assigned. After careful examination and attempts to assign a monoclinic space group, it was decided that the triclinic cell was correct. Examination of the $h0l$ and $-h0l$ ($h0l$ and $h0\bar{l}$) reflections (after absorption correction) indicated that no symmetrical relationship was present. It is suggested that the sample undergoes a second-order phase transition at or before 110 K (monoclinic → triclinic), which is consistent with the known behavior of molecular solids.

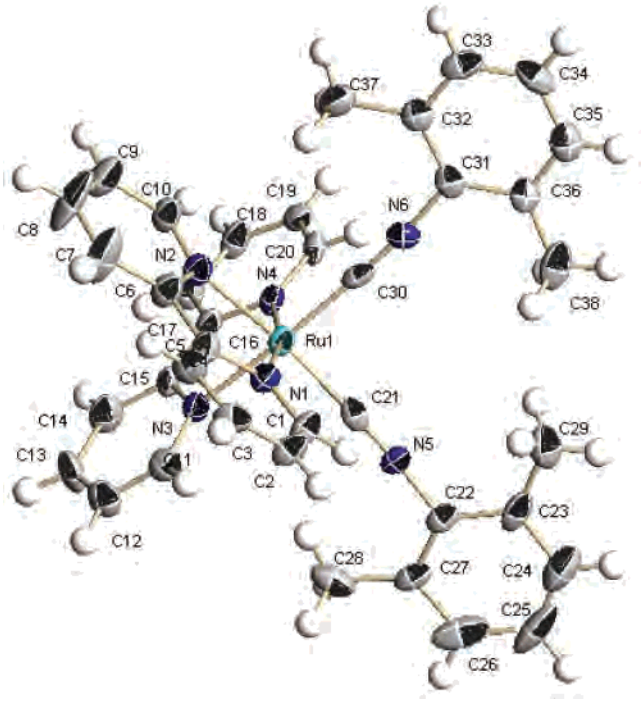

Figure 2. ORTEP diagram of **3**.

Table 2. Selected Bond Lengths (Å) and Angles (deg) for $[Ru(bpy)_2(CNx)_2](PF_6)_2$, **3**

Ru(1)−N(1)	2.079(6)	Ru(1)−C(30)	1.925(10)
Ru(1)−N(2)	2.109(6)	N(5)−C(21)	1.165(9)
Ru(1)−N(3)	2.104(6)	N(5)−C(22)	1.395(11)
Ru(1)−N(4)	2.064(6)	N(6)−C(30)	1.164(10)
Ru(1)−C(21)	1.949(9)	N(6)−C(31)	1.398(11)

C(21)−Ru(1)−N(1)	97.4(3)	N(1)−Ru(1)−N(3)	92.5(2)
C(21)−Ru(1)−N(2)	174.4(3)	N(1)−Ru(1)−N(4)	166.5(2)
C(21)−Ru(1)−N(3)	91.2(3)	N(2)−Ru(1)−N(3)	85.5(2)
C(21)−Ru(1)−N(4)	93.5(3)	N(2)−Ru(1)−N(4)	90.3(2)
C(30)−Ru(1)−N(1)	90.7(3)	N(3)−Ru(1)−N(4)	79.3(2)
C(30)−Ru(1)−N(2)	92.9(3)	C(21)−N(5)−C(22)	176.5(7)
C(30)−Ru(1)−N(3)	176.0(3)	C(30)−N(5)−C(31)	172.3(8)
C(30)−Ru(1)−N(4)	97.1(3)	Ru(1)−C(21)−N(5)	177.2(7)
C(30)−Ru(1)−C(21)	90.7(3)	Ru(1)−C(30)−N(6)	177.6(7)
N(1)−Ru(1)−N(2)	78.3(2)		

strong electron σ-donating and π-withdrawing effects of the CNx ligand with metal centers. This was evident by the shorter Ru−C(CNx) bond lengths in comparison to the bond distances of Ru−N trans to the CNx. The Ru−C(CNx) bond lengths of 1.925(10) and 1.949(9) Å for Ru(1)−C(30) and Ru(1)−C(21), respectively, are comparable to other metal−C(isocyanide) bond lengths found in the literature.[24,25] The bond distances of 1.165(9) and 1.164(10) Å for N(5)−C(21) and N(6)−C(30), respectively, are similar to lengths of C≡N triple bonds reported for other metal−isocyanide systems.[26]

Electronic Absorption Studies. The electronic absorption properties of the prepared complexes were studied at room temperature in ethanol as the solvent. Beer's law studies were conducted using at least five dilution points to determine the absorption coefficients. The probable assignment of these bands was made on the basis of the well-documented optical transitions in $[Ru(bpy)_3]^{2+}$.[27,28] The experimental results are listed in Table 3. The MLCT band underwent a sequential blue shift from **1** to **3** compared to the MLCT band of $[Ru(bpy)_3]^{2+}$ located at 450 nm (Figure 3A).

Table 3. Experimental Electronic Transitions and Simulated Peak Energies of Ru(II) Complexes in EtOH

E (x10^3 cm^{-1}), ϵ (M^{-1} cm^{-1})		
experimental	simulated	assignment
	Complex **1**	
24.4 (8600)	24.4[a] (11100)	MLCT
35.0 (53700)	35.5 (94900)	LC ($\pi \rightarrow \pi^*$)
	Complex **2**	
25.6 (8000)	25.8 (12000)	MLCT
35.2 (47100)	35.7 (85800)	LC ($\pi \rightarrow \pi^*$)
40.0 (26300)		LC ($\pi \rightarrow \pi^*$)
49.0 (52400)		LC ($\pi \rightarrow \pi^*$)
	Complex **3**	
29.1 (7900)	27.1 (11600)	MLCT
31.6 (23700)		LC ($\pi \rightarrow \pi^*$)
32.9 (25000)		LC ($\pi \rightarrow \pi^*$)
36.8 (49900)	36.9 (101300)	LC ($\pi \rightarrow \pi^*$)
	$[Ru(bpy)_3]Cl_2$	
22.2 (12700)		MLCT
35.0 (73400)		LC ($\pi \rightarrow \pi^*$)
39.4 (24100)		LC ($\pi \rightarrow \pi^*$)
40.6 (26100)		LC ($\pi \rightarrow \pi^*$)

[a] Corrected according to procedures given in ref 18d.

Computational Studies. The geometries of the cations of **1**−**3** were optimized for the singlet ground state in the gas phase using the B3LYP[29] functional of the Gaussian 03[30] program package (Table 4). The Stuttgart−Dresden (SDD) effective core potential (ECP)[31] was used for the Ru core potentials. The (8s7p6d)/[6s5p3d] Gaussian-type orbital (GTO) was applied for the valence shell of Ru, together with the all-electron 6-311G* basis set[32] for N, C, Cl, and H atoms.

(24) Lai, S.-W.; Lam, H.-W.; Lu, W.; Cheung, K.-K.; Che, C.-M. *Organometallics* **2002**, *21*, 226.
(25) (a) Tanase, T.; Ukaji, H.; Kudo, Y.; Ohno, M.; Kobayashi, K.; Yamamoto, Y. *Organometallics* **1994**, *13*, 1374. (b) Yamamoto, Y.; Takahashi, K.; Yamazaki, H. *Chem. Lett.* **1985**, 201.
(26) (a) Jovanovic, B.; Manojlovic-Muir, Lj.; Muir, K. W. *J. Chem. Soc., Dalton Trans.* **1972**, 1178. (b) Mann, K. R.; Thich, J. A.; Bell, R. A.; Coyle, C. L.; Gray, H. B. *Inorg. Chem.* **1980**, *19*, 2462.
(27) (a) Rillema, D. P.; Taghdiri, D. G.; Jones, D. S.; Keller, C. D.; Worl, L. A.; Meyer, T. J.; Levy, H. A. *Inorg. Chem.* **1987**, *26*, 578. (b) Rillema, D. P.; Mack, K. B. *Inorg. Chem.* **1982**, *21*, 3849.
(28) Rillema, D. P.; Callahan, R. W.; Mack, K. B. *Inorg. Chem.* **1982**, *21*, 2589.
(29) (a) Becke, A. D. *J. Chem. Phys.* **1993**, *98*, 5648. (b) Lee, C.; Yang, W.; Parr, R. G. *Phys. Rev. B* **1988**, *37*, 785. (c) Vosko, S. H.; Wilk, L.; Nusair, M. *Can. J. Phys.* **1980**, *58*, 1200.
(30) Frisch, M. J.; Trucks, G. W.; Schlegel, H. B.; Scuseria, G. E.; Robb, M. A.; Cheeseman, J. R.; Montgomery, J. A., Jr.; Vreven, T.; Kudin, K. N.; Burant, J. C.; Millam, J. M.; Iyengar, S. S.; Tomasi, J.; Barone, V.; Mennucci, B.; Cossi, M.; Scalmani, G.; Rega, N.; Petersson, G. A.; Nakatsuji, H.; Hada, M.; Ehara, M.; Toyota, K.; Fukuda, R.; Hasegawa, J.; Ishida, M.; Nakajima, T.; Honda, Y.; Kitao, O.; Nakai, H.; Klene, M.; Li, X.; Knox, J. E.; Hratchian, H. P.; Cross, J. B.; Adamo, C.; Jaramillo, J.; Gomperts, R.; Stratmann, R. E.; Yazyev, O.; Austin, A. J.; Cammi, R.; Pomelli, C.; Ochterski, J. W.; Ayala, P. Y.; Morokuma, K.; Voth, G. A.; Salvador, P.; Dannenberg, J. J.; Zakrzewski, V. G.; Dapprich, S.; Daniels, A. D.; Strain, M. C.; Farkas, O.; Malick, D. K.; Rabuck, A. D.; Raghavachari, K.; Foresman, J. B.; Ortiz, J. V.; Cui, Q.; Baboul, A. G.; Clifford, S.; Cioslowski, J.; Stefanov, B. B.; Liu, G.; Liashenko, A.; Piskorz, P.; Komaromi, I.; Martin, R. L.; Fox, D. J.; Keith, T.; Al-Laham, M. A.; Peng, C. Y.; Nanayakkara, A.; Challacombe, M.; Gill, P. M. W.; Johnson, B.; Chen, W.; Wong, M. W.; Gonzalez, C.; Pople, J. A. *Gaussian 03*, revision B.03; Gaussian, Inc.; Pittsburgh, PA, 2003.
(31) Andrae, D.; Hauessermann, U.; Dolg, M.; Stoll, H.; Preuss, H. *Theor. Chim. Acta* **1990**, *77*, 123.

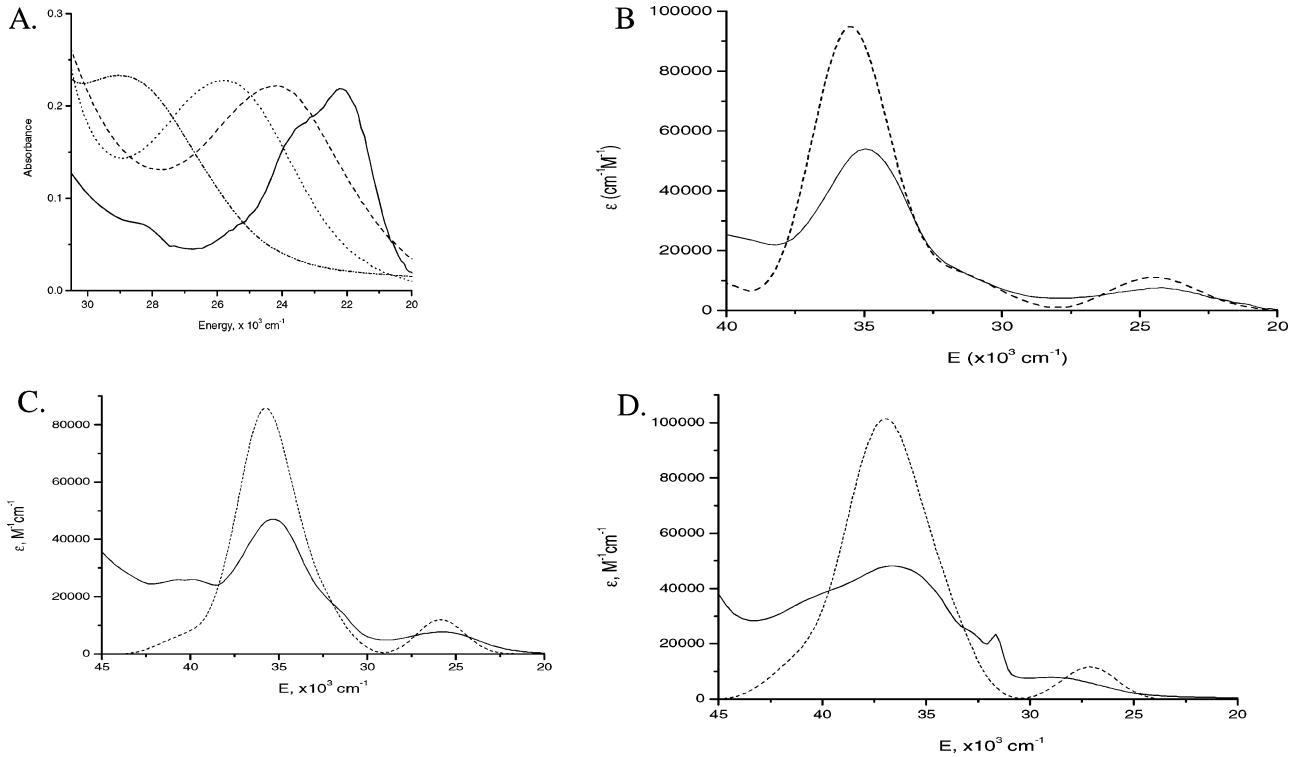

Figure 3. (A) Experimental absorption spectra of the MLCT bands of **1** (- - -), **2** (···), **3** (-··-) and $[Ru(bpy)_3]^{2+}$ (—) in ethanol and experimental UV/vis spectra in ethanol (—) and simulated spectra in ethanol (- - -) of complexes (B) **1**, (C) **2**, and (D) **3**.

Table 4. Selected Geometric Parameters of **1**−**3**

A. Selected Geometric Parameters of **3** Based on Calculated Singlet Ground-State and Lowest-Lying Triplet-State Geometries and X-ray Crystallography[a]

source	Ru−N(1), Å	Ru−N(2), Å	Ru−C(21), Å	N(5)−C(21), Å	C(22)−N(5), Å	Ru−C(21)−N_5, deg	N(1)−Ru−N(2), deg	C(21)−Ru−C(30), deg
X-ray	2.079(6)	2.109(6)	1.949(9)	1.165(9)	1.395(11)	177.2(7)	78.3(2)	90.7(3)
singlet	2.12	2.15	1.94	1.17	1.39	178.4	77.4	92.0
triplet	2.16	2.18	2.01	1.17	1.39	177.1	75.8	93.3

B. Selected Geometric Parameters of **1** and **2** Based on Calculated Singlet Ground-State and Lowest-Lying Triplet-State Geometries[b]

complex	Ru−N(1), Å	Ru−N(2), Å	Ru−C(3), Å	N(4)−C(3), Å	C(5)−N(4), Å	Ru−Cl[−N(py)]	Ru−C(3)−N(5), deg	N(1)−Ru−N(2), deg
singlet **1**	2.10	2.15	1.93	1.17	1.39	2.43	177.7	77.3
triplet **1**	2.09	2.13	1.98	1.16	1.39	2.34	178.2	78.0
singlet **2**	2.11	2.15	1.96	1.17	1.39	2.17	178.5	77.4
triplet **2**	2.38	2.19	1.96	1.17	1.39	2.20	178.2	72.9

[a] Notation according to Figure 2. [b] Notation according to Figure 1.

Nonequilibrium TDDFT[33]/PCM[34] calculations were employed to produce a number of singlet excited states of the complex ions **1**−**3** in ethanol based on the singlet ground-state geometry optimized in the gas phase.[35] The self-consistent reaction field (SCRF) CPCM[36] was used. The output contained information on the excited-state energies and oscillator strengths (*f*), as well as a list of the transitions that give rise to each excited state, the orbitals involved, and the orbital contribution coefficients of the transitions. Selected properties of the singlet excited state with $f > 0.05$ for complexes **1**−**3** are listed in Table 5. Each excited state with $f > 0.01$ (Table S2, Supporting Information) was simulated with a Gaussian curve. The singlet excited states that appear in Table 5 were fit to Gaussian line shapes with maxima equal to the molar absorptivity. The molar absorp-

(32) (a) McLean, A. D.; Chandler, G. S. *J. Chem. Phys.* **1980**, *72*, 5639. (b) Krishnan, R.; Binkley, J. S.; Seeger, R.; Pople, J. A. *J. Chem. Phys.* **1980**, *72*, 650.
(33) (a) Stratmann, R. E.; Scuseria, G. E.; Frisch, M. J. *J. Chem. Phys* **1998**, *109*, 8218. (b) Bauernschmitt, R.; Ahlrichs, R. *Chem. Phys. Lett.* **1996**, *256*, 454. (c) Casida, M. E.; Jamorski, C.; Casida, K. C.; Salahub, D. R. *J. Chem. Phys.* **1998**, *108*, 4439.
(34) Cossi, M.; Barone, V. *J. Chem. Phys.* **2001**, *115*, 4708.
(35) Geometry optimization in solvents was not achieved. Partial optimizations (change in distances of less than 0.001 Å and change in angles of less than 0.01°) followed by TD CPCM calculation produced excited-state energies that were not in better agreement with the experimental excited-state energies than the excited-state energies based on the gas-phase-optimized geometry.
(36) (a) Barone, V.; Cossi, M. J. *Phys. Chem. A* **1998**, *102*, 1995. (b) Cossi, M.; Rega, N.; Scalmani, G.; Barone, V. *J. Comput. Chem.* **2003**, *24*, 669.

Table 5. Calculated Singlet Excited States of **1**−**3** in Ethanol

state	E_{ver}[a] ($\times 10^3$ cm^{-1})	f[b]	$\Psi_o \rightarrow \Psi_v$[c]	type[d]
			1	
4	23.2	0.09	HOMO − 1 → LUMO + 1 (0.6)	Ru_d, Cl → bpy
6	24.5	0.08	HOMO − 2 → LUMO (0.6)	Ru_d, CNx → bpy
17	31.7	0.05	HOMO − 1 → LUMO + 4 (0.5)	Ru_d, Cl → bpy
			HOMO − 1 → LUMO + 6 (0.4)	Ru_{dd}, Cl → CNx
23	33.2	0.05	HOMO − 2 → LUMO + 5 (0.4)	Ru_d, CNx → bpy
			HOMO − 2 → LUMO + 7 (0.3)	Ru_d, CNx → $Ru_{s,d}$
29	34.8	0.16	HOMO − 2 → LUMO + 6 (0.3)	Ru_d, CNx → CNx
			HOMO → LUMO + 9 (0.2)	Ru_d, Cl → $Ru_{s,d}$
30	35.0	0.13	HOMO − 5 → LUMO + 1 (0.4)	Del → bpy
33	35.5	0.20	HOMO − 7 → LUMO + 1 (0.5)	Cl → bpy
34	35.6	0.22	HOMO − 7 → LUMO (0.4)	Cl → bpy
35	35.7	0.48	HOMO − 6 → LUMO (0.3)	bpy $\pi \rightarrow \pi^*$
			HOMO − 7 → LUMO (0.2)	Cl → bpy
36	36.1	0.05	HOMO − 7 → LUMO (0.4)	Cl → bpy
38	36.5	0.05	HOMO − 8 → LUMO + 1 (0.6)	bpy $\pi \rightarrow \pi^*$
44	40.5	0.06	HOMO − 4 → LUMO + 2 (0.5)	bpy $\pi \rightarrow \pi^*$
			2	
5	25.7	0.09	HOMO − 2 → LUMO (0.5)	Ru_d → bpy
6	26.2	0.08	HOMO − 2 → LUMO + 1 (0.4)	Ru_d → bpy
26	34.3	0.06	HOMO − 2 → LUMO + 4 (0.4)	Ru_d → bpy
			HOMO → LUMO + 6 (0.4)	Ru_d, CNx → bpy
30	34.6	0.13	HOMO − 5 → LUMO (0.3)	bpy $\pi \rightarrow \pi^*$
			HOMO − 2 → LUMO + 6 (0.3)	Ru_d → bpy
32	35.1	0.06	HOMO − 2 → LUMO + 6 (0.3)	Ru_d → bpy
			HOMO → LUMO + 9 (0.3)	Ru_d → Del
33	35.5	0.10	HOMO − 6 → LUMO + 1 (0.3)	Del → bpy
			HOMO → LUMO + 6 (0.3)	Ru_d, CNx → bpy
34	35.9	0.40	HOMO − 2 → LUMO + 5 (0.4)	Ru_d → bpy
			HOMO − 5 → LUMO (0.3)	bpy $\pi \rightarrow \pi^*$
35	36.2	0.42	HOMO − 2 → LUMO + 6 (0.4)	Ru_d → bpy
37	37.4	0.05	HOMO → LUMO + 8 (0.3)	Ru_d, CNx → py
			HOMO − 1 → LUMO + 10 (0.3)	Ru_d → Del
38	37.7	0.05	HOMO − 7 → LUMO (0.4)	py → bpy
40	37.9	0.08	HOMO − 1 → LUMO + 10 (0.3)	Ru_d → Del
			HOMO → LUMO + 7 (0.3)	Ru_d, CNx → CNx
49	40.7	0.06	HOMO − 5 → LUMO + 2 (0.5)	bpy $\pi \rightarrow \pi^*$
			3	
4	27.2	0.07	HOMO − 1 → LUMO (0.4)	Ru_d, CNx → bpy
			HOMO → LUMO + 1 (0.4)	Ru_d, CNx → bpy
13	33.6	0.08	HOMO − 1 → LUMO + 2 (0.4)	Ru_d, CNx → bpy
			HOMO → LUMO + 2 (0.3)	Ru_d, CNx → bpy
14	33.8	0.12	HOMO − 5 → LUMO + 1 (0.4)	bpy $\pi \rightarrow \pi^*$
17	34.1	0.07	HOMO − 6 → LUMO (0.4)	bpy $\pi \rightarrow \pi^*$
			HOMO − 7 → LUMO + 1 (0.3)	Del → bpy
24	35.4	0.18	HOMO → LUMO + 4 (0.4)	Ru_d, CNx → CNx, bpy
			HOMO → LUMO + 5 (0.4)	Ru_d, CNx → bpy, CNx
27	35.8	0.16	HOMO − 2 → LUMO + 2 (0.4)	Ru_d → bpy
			HOMO → LUMO + 6 (0.3)	Ru_d, CNx → bpy, CNx
28	36.1	0.13	HOMO → LUMO + 5 (0.4)	Ru_d, CNx → bpy, CNx
			HOMO → LUMO + 4 (0.3)	Ru_d, CNx → CNx, bpy
30	36.4	0.05	HOMO − 2 → LUMO + 3 (0.4)	Ru_d → bpy
			HOMO − 1 → LUMO + 5 (0.3)	Ru_d, CNx → bpy, CNx
33	36.8	0.22	HOMO → LUMO + 6 (0.4)	Ru_d, CNx → bpy, CNx
34	37.0	0.15	HOMO − 1 → LUMO + 7 (0.4)	Ru_d, CNx → Del
35	37.4	0.14	HOMO → LUMO + 6 (0.3)	Ru_d, CNx → bpy
			HOMO → LUMO + 9 (0.3)	Ru_d, CNx → Del
36	37.7	0.15	HOMO − 2 → LUMO + 7 (0.4)	Ru_d → Del
			HOMO → LUMO + 7 (0.4)	Ru_d, CNx → Del
37	37.8	0.21	HOMO − 2 → LUMO + 4 (0.3)	Ru_d → CNx, bpy
			HOMO − 2 → LUMO + 5 (0.4)	Ru_d → bpy, CNx
39	38.2	0.09	HOMO − 2 → LUMO + 6 (0.4)	Ru_d → bpy, CNx
41	38.4	0.08	HOMO − 3 → LUMO + 5 (0.3)	CNx → bpy, CNx
			HOMO − 4 → LUMO + 5 (0.3)	CNx → bpy, CNx
45	39.2	0.11	HOMO − 2 → LUMO + 9 (0.3)	Ru_d → Del
			HOMO − 1 → LUMO + 7 (0.3)	Ru_d, CNx → Del
46	39.4	0.09	HOMO → LUMO + 7 (0.3)	Ru_d, CNx → Del
			HOMO − 2 → LUMO + 9 (0.3)	Ru_d → Del

[a] E_{ver} is the energy of the vertical transition. [b] f is the oscillator strength. [c] ψ_o and ψ_v are, respectively, the occupied and the virtual orbitals that define the transition. The absolute value of the transition coefficient for each transition is given in parentheses. [d] The transition type is determined on the basis of the change in the spatial distribution from occupied to virtual orbital. Del = delocalized. (See text for calculation details.)

Table 6. Emission Properties of the Complexes in 4:1 (v/v) EtOH/MeOH at 77 K and Computed Lowest-Lying Triplet-State Energies

complex	E_{77K},[a] $\times 10^3$ cm^{-1}	τ_{em}, μs	E_{LLTS}, $\times 10^3$ cm^{-1}
1	17.2, 16.1 (sh)	3.2	16.1
2	19.2, 17.9, 16.7 (sh)	8.0	17.1
3	21.8, 20.4, 19.2 (sh), 17.6 (sh)	25	21.8
$[Ru(bpy)_3]Cl_2$	17.4, 16.1	7.2	18.2

[a] sh = shoulder.

tivity was calculated with a full width at half-maximum of 3300 cm^{-1}. The integrated Gaussian curves are shown in Figure 3.[18a]

The TDDFT/CPCM calculations are nonequilibrium calculations with respect to the polarization process between the solvent reaction field and the charge density of the electronic state indicated in the input. For singlet excited states, this is the singlet ground state.[37a] The CPCM is designed to account for the bulk physical properties of the solvent; it does not account for specific solvent−solute interactions. The TDDFT is known to perform well for the computing of CT excited states between closely spaced moieties. The tandem use of CPCM and TDDFT is currently the most suitable computational approach for the treatment of solvent effects on the transition metal complexes excited-state energies.[18d]

The lowest-lying triplet-state geometries of the series were calculated using unrestricted B3LYP in the gas phase (Table 4). The spin contamination from states of higher multiplicity was low. The value of $\langle S^2 \rangle$ was 2.009 for complex **1**, 2.013 for complex **2**, and 2.019 for complex **3**. The energies of the lowest-lying triplet states were higher than those of the corresponding ground states by 16100 cm^{-1} for complex **1**, 17100 cm^{-1} for complex **2**, and 21800 cm^{-1} for complex **3** (Table 6). The lowest-lying triplet states were MLCT states and featured single HOMO and LUMO occupancies.

A number of triplet excited states were calculated on the basis of the geometry of the lowest-lying triplet state. The results from this calculation are presented in Table 7. The excited-state energies are given relative to the energy of the lowest-lying triplet state.

Vibrational analysis was performed using the DFT method for the three complexes in the singlet ground-state geometries. The frequencies of the most intense vibrations are listed in Table 8.

Electrochemical Studies. The redox potentials of the complexes in the series were determined by cyclic voltammetry. The electrochemical properties of the complexes are listed in Table 9. An irreversible oxidation and a closely following reversible one were observed for **1** at 0.99 and 1.12 V, respectively. The irreversible wave is attributable to oxidation of chloride ion, whereas the reversible wave is due to the Ru(III)/(II) redox couple. This is not the pattern that was observed for the other two complexes. The oxidation waves of **2** were reversible, and those of **3** were irreversible; both were shifted to more positive potential relative to $[Ru(bpy)_3]^{2+}$.

The complexes exhibited two reversible reduction processes attributed to the stepwise reduction of the two 2,2′-bipyridine ligands. The cyclic voltammogram waves were slightly shifted to more positive potentials in the order **1** < **2** < **3**.

Emission Properties and Excited-State Lifetimes. The complexes were nonemissive at room temperature but were highly emissive at 77 K (Figure 4). The emission maxima were located at higher energy than that observed for $[Ru(bpy)_3]^{2+}$ and the spectra displayed structured emission resulting from vibronic coupling.[38] The emission lifetimes of the complexes at 77 K in 4:1 (v/v) ethanol/methanol ranged from 3.2 μs for **1** to 25 μs for **3**. Results of the emission and excited-state lifetime studies are reported in Table 6.

After the wavelength (abscissa) values had been converted to energies, the emission spectral data were fit to eq 1

$$I(E) = I_0 + A\left(\sum_{n_1}\sum_{n_2}\left[\frac{(E_0 - n_1\hbar\omega_1 - n_2\hbar\omega_2)}{E_0}\right]^4\left(\frac{S_1^{n_1}}{n_1!}\right)\times \left(\frac{S_2^{n_2}}{n_2!}\right)\exp\left\{-4(\log 2)\left[\frac{(E - E_0 + n_1\hbar\omega_1 + n_2\hbar\omega_2)}{\upsilon_{1/2}}\right]^2\right\}\right) \quad (1)$$

where the summation is carried out over the two sets of six vibrational levels.[39] The parameters are as follows: $I_0 = 0$; n_1, $n_2 = 0-5$; A is the peak area; E_0 is the 0−0 energy; $\hbar\omega_1$ and $\hbar\omega_2$ represent the energies of the high- and low-frequency vibrational acceptor modes, respectively; S_1 and S_2 are measures of the distortion in the high- and low-frequency acceptor modes, respectively; and $\upsilon_{1/2}$ is the full width at half-maximum of the 0−0 vibronic component in the emission spectra. The maximum intensity was adjusted to 1 for the curve-fitting analysis.

The spatial distribution of the singly occupied orbitals in the excited state can be determined from the vibrational frequency acceptor modes. For example, for the MLCT state, the high-frequency acceptor mode would be the ligand ring-breathing mode, and the low-frequency acceptor mode would be related to the vibrations of metal−ligand bonds. The coefficients S_1 and S_2 are indicative of the relative contributions of the high- and low-frequency vibrational modes to the fine vibronic structure of the emission.

The results of the emission spectral curve fitting at 77 K (Figure 4) are listed in Table 10. The values of the high-frequency modes at about 1500 cm^{-1} corresponding to the ring-breathing modes for the complexes are consistent with the location of the excited states on the bpy ligand. The low-frequency modes were attributed to metal−ligand vibrations.

(37) (a) Frisch, E.; Frisch, M. J.; Trucks, G. W. *Gaussian 03 User's Reference, version 7.0*; Gaussian Inc.: Pittsburgh, PA, 2003; p 206. (b) Foresman, J. B.; Frisch, Æ. *Exploring Chemistry with Electronic Structure Methods*, 2nd ed.; Gaussian Inc.: Pittsburgh, PA, 1996; p 215, 259−260.

(38) Drago, R. S. *Physical Methods for Chemist*, 2nd ed.; Saunders College Publishing: Orlando, FL, 1992; p 124.

(39) (a) Caspar, J. V. Ph.D. Thesis, University of North Carolina, Chapel Hill, North Carolina, 1982. (b) Allen, G. H.; White, R. P.; Rillema, D. P.; Meyer, T. J. *J. Am. Chem. Soc.* **1984,** *106*, 2613.

Table 7. Calculated Triplet Excited States of **1**−**3** in Ethanol Based on the Lowest-Lying Triplet-State Geometry

state	f[a]	$\psi_o \rightarrow \psi_v$[b]	type[c]	E_{ver}[d] ($\times 10^3$ cm^{-1})
		1		
1	0.0088	LUMO → LUMO + 1 (0.6)	$\pi \rightarrow \pi^*$ (bpy)	1.1
2	0.0007	HOMO − 1 → HOMO (0.6)	Ru_d, Cl → Ru_d, Cl	2.2
		HOMO − 2 → HOMO (0.6)	Ru_d, CNx → Ru_d, Cl	
3	0.0001	HOMO − 1 → HOMO (0.3)	Ru_d, Cl → Ru_d, Cl	4.2
		HOMO − 2 → HOMO (0.7)	Ru_d, CNx → Ru_d, Cl	
		2		
1	0.0003	HOMO − 1 → HOMO (0.7)	$Ru_d \rightarrow Ru_d$, CNx	4.8
		HOMO − 2 → HOMO (0.7)	$Ru_d \rightarrow Ru_d$, CNx	
2	0.0009	HOMO − 1 → HOMO (0.7)	$Ru_d \rightarrow Ru_d$, CNx	6.0
		HOMO − 2 → HOMO (0.7)	$Ru_d \rightarrow Ru_d$, CNx	
		3		
1	0.0015	HOMO − 2 → HOMO (0.8)	$Ru_d \rightarrow$ CNx, Ru_d	3.5
2	0.0089	HOMO − 1 → HOMO (0.7)	CNx, $Ru_d \rightarrow$ CNx, Ru_d	4.2
		HOMO − 6 → HOMO (0.5)	$\pi \rightarrow \pi^*$ (bpy)	
3	0.0186	HOMO − 1 → HOMO (0.7)	CNx, $Ru_d \rightarrow$ CNx, Ru_d	5.3
		HOMO − 6 → HOMO (0.5)	$\pi \rightarrow \pi^*$ (bpy)	
4	0.0011	LUMO → LUMO + 1 (1.0)	$\pi \rightarrow \pi^*$ (bpy)	6.0

[a] f is the oscillator strength. [b] ψ_o and ψ_v are, respectively, the occupied and the virtual orbitals that define the transition. The absolute value of the transition coefficient for each transition is given in parentheses. [c] The transition type is determined on the basis of the change in the spatial distribution from occupied to virtual orbital. (See text for calculation details.) [d] E_{ver} is the energy of the vertical transition, relative to the lowest-lying triplet-state energy.

Table 8. Calculated Vibrational and Experimental Infrared Frequencies for the Three Complexes

1		**2**		**3**		
calc[a]	expt	calc[a]	expt	calc[a]	expt	assignment[b]
2185 (1355)	2088	2195 (730)	2104	2230 (667)	2155	a
−	−	−	−	2202 (667)	2115	a
1640 (11)	1653	1637 (18)	1653	1637 (26)	1653	b
1637 (8)	1636	1635 (21)	1647	1635 (25)	1635	b
1513 (22)	1559	1515 (24)	1521	1513 (35)	1518	b
1505 (49)	1540	1502 (30)	1507	1502 (25)	1506	b
1497 (66)	1507	1498 (65)	1471	1495 (62)	1471	b
783 (80)	771	790 (86)	762	787 (96)	763	c
778 (73)	731	789 (100)	732	786 (96)	731	c
516 (35)	510	514 (33)	511	514 (19)	508	d
−	−	−	−	509 (27)	501	d

[a] Calculated relative intensities given in parentheses. [b] a = CN stretch, b = bpy ring-breathing modes, c = out-of-plane H (bpy) vibrations, d = CNx vibrations.

Table 9. Electrochemical Properties of the Complexes in CH_3CN at Room Temperature

complex	$E_{1/2}$, V[a]	$E_{1/2}$, V[a](L)
1	0.99[b]	−1.44
	1.12[c]	−1.63
2	1.65[c]	−1.27
		−1.47
3	1.54[b]	−1.24
		−1.45
$[Ru(bpy)_3]^{2+}$[14]	1.27[c]	−1.31
		−1.50
		−1.77

[a] Potential vs SSCE (scan rate = 250 mV/s). [b] Irreversible oxidation wave. [c] Ru(III)/(II) redox couple.

Discussion

Geometry Optimization of 3. Results of the singlet and triplet geometry optimizations of complex **3** in the gas phase in comparison to the selected X-ray data are presented in Table 4A. Good agreement for the bond lengths of Ru−C(21), N(5)−C(21), and N(5)−C(22) was achieved for the optimized singlet ground-state geometry in comparison to the X-ray data. The shorter Ru−N(1) distance and the longer Ru−N(2) distance are reasonable considering the electron σ-donor/π-withdrawing ability of the CNx ligands and are in accord with the X-ray results. The calculated Ru−N bonds are longer than the experimental values by 0.04 Å. The results obtained here with one of the largest basis sets appear satisfactory despite the shortcomings associated with the calculation of the metal−ligand bond lengths using B3LYP theory.[18a−c]

Most geometric parameters did not change significantly in the lowest-lying triplet state compared to the singlet ground state. For example, the bond distances for N(5)−C(21) and N(5)−C(22) of 1.17 and 1.39 Å, respectively, are the same. Some did change, however. For example, metal−ligand distances were from 0.03 Å for Ru−N(2) to 0.07 Å for Ru−C(21) longer in the triplet state relative to the ground state. The Ru−C(21)−N(5) and N(1)−Ru-N(2) bond angles were relatively smaller, whereas the C(21)−Ru−C(30) bond angle was larger compared to the ground-state geometry, probably to accommodate the longer ruthenium−ligand bonds. Even though the Ru−N(1) and Ru−N(2) bond distances for the triplet-state geometry were greater than those for the singlet state, the bond length for Ru−N(1) was considerably shorter in comparison to Ru−N(2). The Ru−N bond elongation in the triplet state is related to the decrease of the electron density on the Ru atom and the increase of the electron density on the bpy ligand, resulting in a weaker Ru−N bond.

Geometry Optimization of 1 and 2. The results from the geometry optimizations of **1** and **2** in the singlet ground state and the lowest-lying triplet state are listed in Table 4B. The calculated Ru−N(2) bond distances are longer than the Ru−N(1) bond distances, in accord with the trans electronic effect of the isocyanide ligand (Figure 1). The Ru−Cl bond is slightly longer than the 2.40 Å value reported for $[Ru(bpy)_2(CN)Cl]$.[40a] The Ru−N(py) bond is longer than the 2.10 Å reported for $[Ru(bpy)_2(py)_2](PF_6)_2$,[40b] which might be due to electronic neighboring effects of CNx.

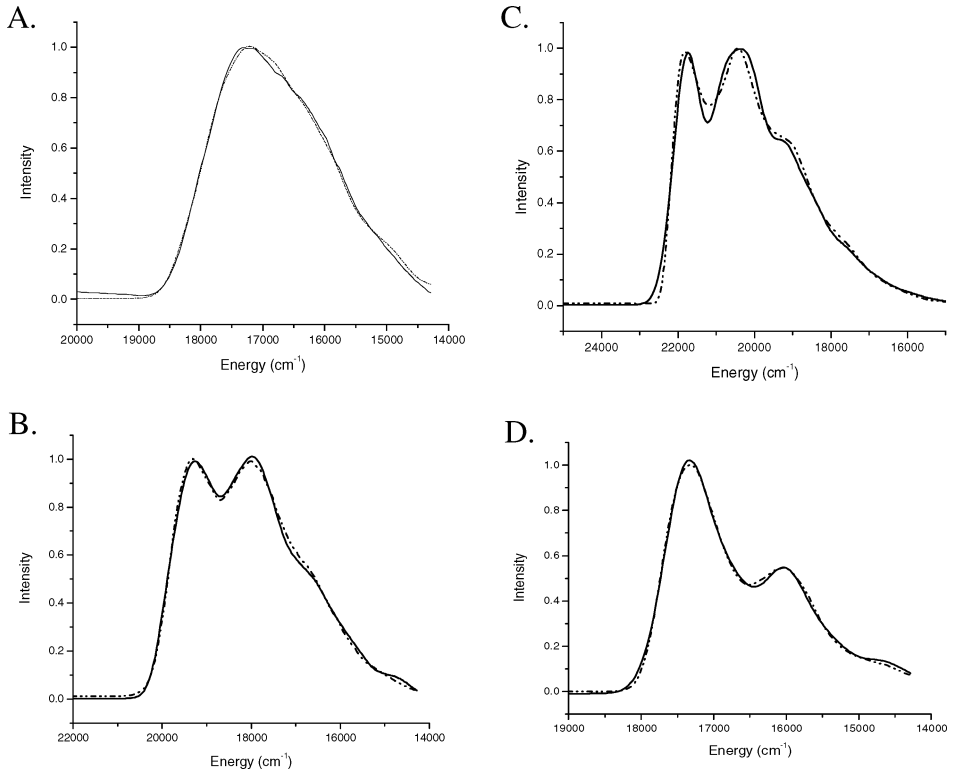

Figure 4. Corrected emission spectra (–) of (A) **1**, (B) **2**, (C) **3**, and (D) $[Ru(bpy)_3]^{2+}$ and experimental emission (-···-) in 4:1 (v/v) EtOH/MeOH at 77 K. Maximum intensity was adjusted to 1 for the curve-fitting analysis.

Table 10. Emission Spectral Curve Fitting Parameters[a] in 4:1 (v/v) EtOH/MeOH at 77 K[a]

complex	E_{em}, cm^{-1}	E_0, cm^{-1}	$\hbar\omega_1$, cm^{-1}	S_1	$\hbar\omega_2$, cm^{-1}	S_2	$v_{1/2}$	A
1	17240	18150	1440	0.46	446	2.75	605	0.23
2	19230	19800	1450	1.18	420	1.87	637	0.39
3	21830	21760	1570	0.87	948	0.91	852	0.95
$[Ru(bpy)_3]^{2+}$	17360	17380	1370	0.61	624	0.48	736	0.97

[a] Error limits are as follows: E_0, ±20 cm^{-1}; $\hbar\omega$, ±10 cm^{-1}; S_1, S_2, ±0.02; $v_{1/2}$, ±28 cm^{-1}; A, ±0.01.

In the lowest-lying triplet state of **1**, the Ru−Cl bond is about 4% shorter than in the singlet ground state. As in **3**, the Ru−C_3 bond is longer in the triplet state. The Ru−N(1) and Ru−N(2) bonds are slightly elongated relative to those in the singlet ground state. In the triplet state of **2**, the Ru−N(1) bond distance was found to increase dramatically (by 0.27 Å), whereas the Ru−N(2) bond distance increased by only 0.04 Å. The Ru−N(1) bond elongation in the triplet state of complex 2 is due to the single electron occupancy of the Ru−N(1) antibonding LUMO. The N(1)−Ru−N(2) angle changed accordingly to accommodate the changes in the metal−bipyridine bond lengths.

Molecular Orbital Analysis. The energies and the spatial distributions of 12 frontier molecular orbitals for the three complexes in the singlet ground state are shown in Figure 5. The highest occupied molecular orbital (HOMO) for **1** is located on the metal center and the chloro ligand, whereas for **2** and **3**, it is located on the metal center and the CNx ligand (Figure 6). The HOMO of **1** is antibonding with respect to the Ru−Cl, whereas the HOMO of **3** is bonding with respect to the Ru−C(CNx) bond. Thus, the calculated Ru−C(isocyanide) bond length for complex **3** is longer in the triplet state by 0.07 Å relative to the ground state, whereas the calculated Ru−Cl bond length in the triplet state decreases by 4% for complex **1**. The bonding and antibonding character was determined by visual examination of the phases of the molecular orbital for each diagram. The phases are related to the spatial distributions of α and β electron

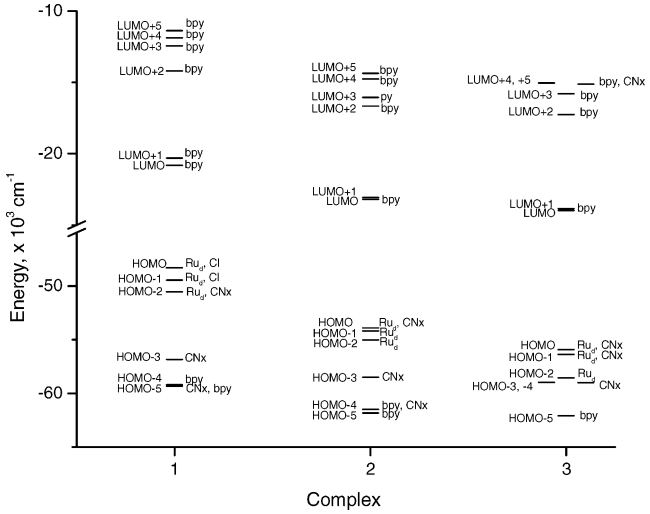

Figure 5. Molecular orbital energy diagram for six frontier occupied and six frontier virtual orbitals of **1**−**3** in the singlet ground state in ethanol.

(40) (a) Clear, J. M.; Kelly, J. M.; O′Connel, C. M.; Vos, J. G.; Cardin, C. J.; Costa, S. R.; Edwards, A. J. *J. Chem. Soc., Chem. Commun.* **1980**, 750. (b) Cordes, A. W.; Durham, B.; Swepston, P. N.; Pennington, W. T.; Condren, S. W.; Jensen, R.; Walsh, J. L. *J. Coord. Chem.* **1982**, *11*, 251.

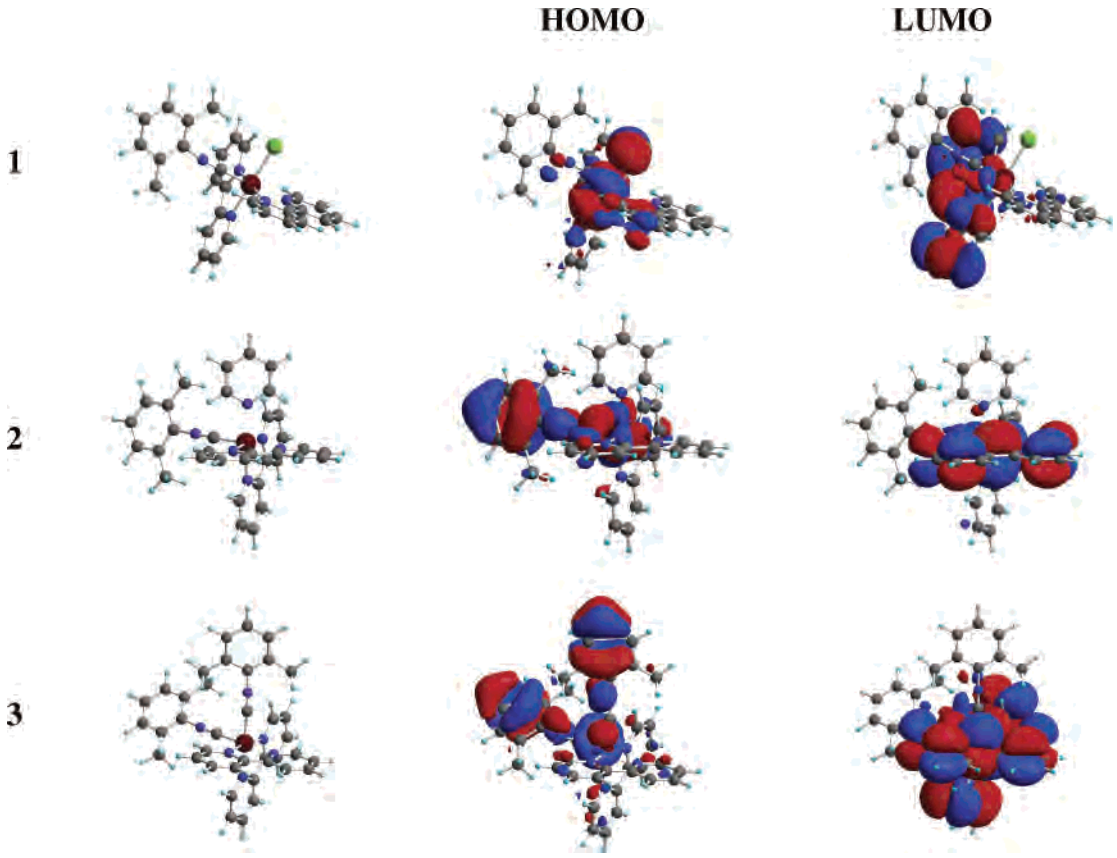

Figure 6. Molecular orbital schemes of the HOMO and LUMO of **1**−**3**.

densities[37b] shown in red and blue, respectively (Figure 6). Occupied lower-energy molecular orbitals are also located mostly on the metal center and the ancillary ligands. The four lowest-energy unoccupied molecular orbitals (LUMOs) for all complexes are located on the bpy or pyridine ligand-(s). The LUMO + 1 orbitals for the series are very close in energy to the LUMOs for **2** and **3**, as the two bipyridine ligands are in approximately the same environment. For example, the LUMO + 1 for complex **1** is 480 cm^{-1} higher in energy than the LUMO, whereas LUMO + 1 and the corresponding LUMO are nearly degenerate for complexes **2** and **3**.

Singlet Excited States. The 50 lowest singlet excited states of **1**−**3** in ethanol were calculated (available in Table S2, Supporting Information), and only those with $f > 0.05$ are listed in Table 5. The excited-state types were determined on the basis of the percent molecular orbital contributions of the orbitals involved in the electronic transition that gives rise to the excited state. The percent contributions are listed in Supporting Information Table S3. For **1**, excited states 4−17 involve mostly transitions from Ru_d and Cl orbital components (HOMO and HOMO − 1) to bpy (LUMO to LUMO + 5) and can be classified as (metal−ligand)-to-ligand charge transfer (MLLCT) (Figures 5 and 6). State 23 involves CNx ligand and Ru_d orbitals. The higher-energy states are associated with bpy $\pi \rightarrow \pi^*$ and Cl-to-bpy charge-transfer transitions. These states feature high f values. The virtual orbitals for the transitions to the excited states of **1** are mostly located on the bpy ligands.

Low-energy excited states 5 and 6 of complex **2** are based on transitions from the Ru_d-centered orbitals HOMO − 1 and HOMO − 2 to the bpy-centered orbitals LUMO and LUMO + 2. These excited states were assigned as MLCT. For the higher-energy excited states, the occupied orbitals that give rise to the transitions are of mixed metal and isocyanide character, whereas the virtual orbitals are mostly bpy-centered. A number of bpy $\pi \rightarrow \pi^*$ transitions with high f were assigned from 36000 cm^{-1} to 40000 cm^{-1}.

Upon addition of the second CNx ligand in **3**, the contribution of the CNx moiety to the occupied orbitals HOMO and HOMO − 1 is almost as high as the metal contribution, whereas the virtual orbitals are situated on the bpy moiety (Figures 5 and 6). Hence, excited states 4 and 13 that involve the above occupied orbitals were assigned as MLLCT. The higher-energy excited states of **3** are similar to those of complexes **1** and **2**.

Mulliken Atomic Charges. The Mulliken atomic charges were computed in ethanol. The Mulliken charges on Ru decrease significantly with CNx substitution. The charge on ruthenium decreases from 1.44 for the standard, $[Ru(bpy)_3]^{2+}$, to 0.96 for the bis CNx-substituted complex. The charge lowering can be related linearly to the coordinating atoms as follows: $Ru^{calc} = Ru^{2-[nL+(6-n)L']}$, where n represents the number of coordinating atoms from ligand L and $6 - n$ corresponds to the number of coordinating atoms from ligand L′. The contribution for each nitrogen atom in $[Ru(bpy)_3]^{2+}$ is ∼0.1, giving $Ru^{1.44}$ from $Ru^{2-[6(0.1)]}$. For $[Ru(bpy)_2(CNx)_2]^{2+}$, $Ru^{0.96} = Ru^{2-[4(0.1)+(2y)]}$, the contribution per CNx

ligand is ~0.32. Using $L = 0.1$ for the five coordinating N atoms and $L' = 0.32$ for the coordinating CNx ligand in the relationship $Ru^{calc} = Ru^{2-[nL+(6-n)L']}$ yields an Ru^{calc} value of 1.18 for complex **2** compared to the DFT-calculated Ru atom charge of 1.17.

Complex **1** featured the lowest metal charge of 0.89 because of the presence of the chloride ligand. These Mulliken charges can be related to the shifts in the electrochemical reduction potentials of the complexes.

Electronic Absorption Behavior. Although the complexes showed typical MLCT transitions consistent with the ruthenium(II) polypyridyl systems,[41] they underwent large hypsochromic (blue) shifts (Figure 3A). The MLCT peak shifted from 24400 cm^{-1} for **1** to 25600 cm^{-1} for **2** when chloride was replaced with pyridine in the coordination sphere. An even larger shift to 29100 cm^{-1} was observed for **3** when the second CNx ligand entered the coordination sphere (Table 3). The shift is a consequence of the increasing HOMO−LUMO energy difference in the order **1** < **2** < **3** as a result of higher π-acceptor ability and stronger σ-donor ability of the isocyanide ligand relative to bpy. The MLCT peak energies for the three complexes follow the same general trend as the simulated MLCT peak energies (Table 3 and Figure 3B−D).

Intense peaks (ϵ of about 50000 $M^{-1}cm^{-1}$) were observed at about 35000 cm^{-1} for the three complexes. These were assigned as bpy ligand-centered (LC) transitions on the basis of past reports.[27,28]

The positions and the assignments based on the singlet excited states of the simulated peaks are listed together with the experimental absorption energies in Table 3. Using the calculated singlet excited states in ethanol in Table 5, simulated absorption spectra of the three complexes were determined and are overlaid with the experimental results (Figure 3B−D). The correlation between the experimental and calculated spectra of **1** in the range 30000−34000 cm^{-1} is impressive. Very good agreement between experimental and simulated spectra was also produced for complex **2** in the 30000−34000 cm^{-1} energy range. The CT maximum for **1** was corrected from 23600 cm^{-1} to 24400 cm^{-1} using previously reported procedures based on the solvent dependence of the CT band.[18d]

The simulated MLCT and higher-energy peaks of **2** deviate by less than 500 cm^{-1} from the experimental results. The largest difference between simulated and experimental spectra is observed for the CT peak of **3**. The experimental CT peak is shifted by about 1900 cm^{-1} toward higher energy. The shift can be attributed to mixing between the lower-energy states 1−6 and the higher-energy states 13 and 15 as they involve transitions of similar type. The most prominent experimental peak of **3** is broad and has a maximum at 36760 cm^{-1} compared to the simulated UV/vis absorption value of 36890 cm^{-1}.

Electrochemical Behavior. The electronic effects of the CNx ligand are evident in the electrochemical results (Table 9). The oxidation potentials varied considerably when bpy was replaced with CNx, Cl, and py. The primary effect is stabilization of the Ru(II) state relative to Ru(III) by a combination of CNx σ and π effects. Interestingly, chloride is first oxidized and then Ru(II) for **1**. According to the calculations, the HOMO is largely Ru_d-based (72%) with a small contribution from the chloro ligand (16%). The irreversible process attributed to chloro ligand oxidation occurs on the shoulder of the reversible oxidation assigned to the Ru(III/II) couple. The fact that the two oxidations occur simultaneously might mean that the chloro ligand remains coordinated to the Ru(III) species produced at the electrode surface giving rise to the observed reversible Ru(III/II) oxidation. For **2** and **3**, the HOMO is located on both the ruthenium and the CNx ligand, with the net result of shifting the oxidations to more positive potential than for $[Ru(bpy)_3]^{2+}$.

Electrochemical reductions occur at the bipyridine ligand as has been reported for other ruthenium(II) polypyridyl complexes.[42] The shift to more positive reduction potentials means that the bpy ligand in **3** is easier to reduce than that in **2**, whereas the bpy ligand in **1** would be the hardest to reduce. This result is supported by the DFT-computed LUMO energies presented in Figure 5. Complex **3**, being the easiest to reduce, has the lowest-lying LUMO, followed by **2**. Complex **1** on the other hand has the highest-lying LUMO. The effects on the reduction of bpy were small because the π^* (bpy) levels are removed from the direct site of Ru−L interaction and can therefore act as "spectator sites".[43] The reduction potentials for the three complexes increase in same order as the Mulliken charges on the Ru atom. Complex **1** has the lowest charge on the Ru atom and the most difficult bpy ligand to reduce within the series, followed by complexes **3** and **2**.

Vibrational Analysis. The calculated vibrational frequencies for the three complexes are given in Table 8 together with the experimental IR results. Only the most distinct and intense peaks are considered for comparison. The most intense vibrations are attributed to the C≡N stretching mode. The IR absorptions at about 1500−1650 cm^{-1} are related to the aromatic ring-breathing modes, mostly of the bpy moiety. The intense vibrations at about 700 cm^{-1} are due to the out-of-plane vibrations of the hydrogen atoms bound to the aromatic rings. The peak at about 500 cm^{-1} is characteristic of CNx ligand vibrations. The computational assignments are in a very good agreement with the conventional ones.

One C≡N stretch is observed for **1** and **2**, but two well-resolved peaks are observed for **3** located 40 cm^{-1} apart. The stretching frequency of C≡N increases as the number of CNx ligands increases and upon replacement of the chloro ligand with pyridine. In like manner, the calculated force constants of the C≡N stretches increase as follows: 36.4 mdyn/Å for **1** < 36.7 mdyn/Å for **2** < 36.9 and 37.9 mDyne/Å for **3**. The calculated C≡N stretching frequencies overestimate the experimental values by 80−100 cm^{-1}. The

(41) Juris, A.; Balzani, V.; Barigelletti, F.; Campagna, S.; Belser, P.; von Zelewsky, A. *Coord. Chem. Rev.* **1988**, *84*, 85.

(42) Morris, D. E.; Hanck, K. W.; DeArmond, M. K. *J. Am. Chem. Soc.* **1983,** *105*, 3032.

calculated separation of the two C≡N vibrational modes of **3** is 28 cm^{-1}. An intense vibration specific to the CNx ligand is located in the lower-energy region of the spectrum. The computational results show that this mode involves the vibration of the CNx moiety with respect to the rest of the complex. The vibrational frequency of CNx for **1** was calculated at 516 cm^{-1}, compared to the experimental value of 510 cm^{-1}. The CNx vibration for **2** was computed at 514 cm^{-1} and experimentally verified at 511 cm^{-1}. Two CNx-specific vibrations were expected for the bis-isocyanide complex **3** at 509 and 514 cm^{-1}. Two experimental IR peaks were indeed resolved for the latter at 501 and 508 cm^{-1}. The agreement between the computed and experimental vibrational frequencies is satisfactory, considering that the computed vibrational frequencies are known to be higher than those observed experimentally.[44]

Triplet Excited States. The triplet excited states presented in Table 7 have low oscillator strength. Some of these states involve triplet transitions from the singly occupied LUMO to LUMO + 1 that are assigned to bpy $\pi \rightarrow \pi^*$ transitions. The majority of the states, however, involve transitions from fully occupied molecular orbitals to the HOMO that was singly occupied in the lowest-lying triple state. The states that involve the fully occupied orbitals HOMO − 1 and HOMO − 2 are assigned as metal-centered d−d states. For complex **1**, triplet excited state 1 is ligand-centered. Excited states 2 and 3 are due to mixed Ru d−d and chloro ligand excitations. Excited states 1 and 2 of complex **2** are primarily d−d states. For complex **3**, the CNx ligand contribution to the occupied orbital HOMO − 1 is higher, and the d−d character of excited states 2 and 3 is not as pronounced as that of excited state 1. States 2 and 3 are also mixed with bpy $\pi \rightarrow \pi^*$ transitions. Excited state 4 is bpy ligand-centered. The geometries of these states are not optimized, and the energies reported are not the minima. The triplet excited states were calculated on the basis of the lowest-lying triplet-state (^{3}MLCT) geometry because, according to Kasha's rule, the ^{3}MLCT state should be the emitting state. The triplet excited states listed in Table 4 were determined on the basis of the most stable triplet geometry. Triplet excited states calculated from the singlet ground-state geometry are multiplicity-forbidden (f=0). The role of the ligand-centered states in the temperature dependence of the emission maxima and of the d−d states in the lack of room-temperature emission is discussed in the next section.

Emission and Excited-State Lifetime Behavior. Figure 7 shows a general kinetic scheme used to explain the observed excited-state dynamic behavior of the standard complex, $Ru(bpy)_3^{2+}$. In this model, the ^{3}MLCT state is populated with unit quantum efficiency ($f = 1$). Once formed, ^{3}MLCT undergoes three decay processes: radiative decay (k_r), nonradiative decay (k_{nr}), and thermal population of a low-lying excited state that undergoes efficient radiationless decay and results in a low-yield photosubstitution reaction.[45]

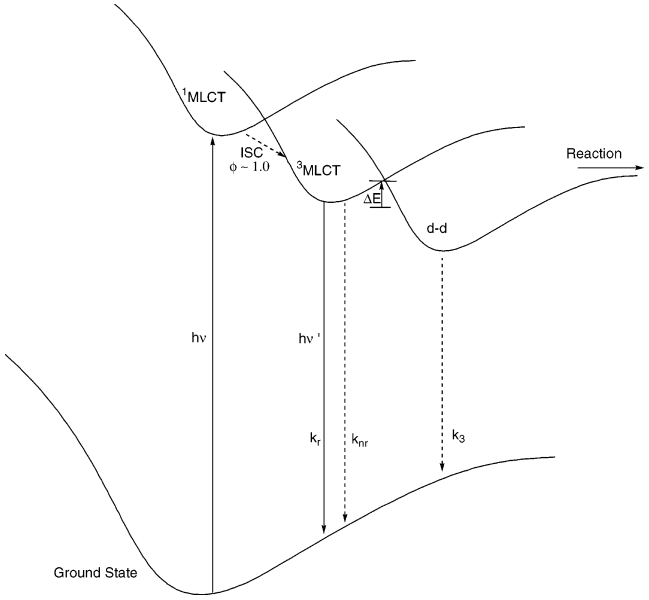

Figure 7. Photophysical processes of $Ru(bpy)_3^{2+}$.

The substitution of CNx for bpy in the parent complex, $Ru(bpy)_3^{2+}$, provided an interesting effect on the excited-state behavior of the complex. The band profile showed the typical MLCT character exhibited by ruthenium(II) polypyridyl complexes,[46] but the low-temperature emission maxima of the series underwent a blue shift. In most cases, the emission was from mixed singlet−triplet excited states.

According to Kasha's rule, the emission occurs from the lowest-lying excited state. Complex **3** features the longest excited-state lifetime, and its lowest-lying triplet-state energy of 21800 cm^{-1} is in excellent agreement with the experimental value. For complexes **1** and **2**, the computed triplet excited-state energies are lower than the experimental values by 1100 and 2100 cm^{-1}, respectively. The calculated lowest-lying triplet excited states arise upon single electron occupation of the respective LUMOs that for the three complexes are located on the bpy moieties (Figure 6). This comparison is made with 77 K experimental data, and it is commonly observed that the emission shifts to higher energy with decreasing temperature.

The emission lifetimes at 77 K decrease from complex **3** to complex **1** in accord with the energy gap law,[47] but emission is lost in fluid solution. This loss is readily explained for **1** as the presence of chloride in the coordination sphere provides a mechanism for nonradiative decay as a result of the heavy-atom effect. A reasonable and self-consistent explanation for the loss of room-temperature emission for **2** and **3** is the enhanced rate of thermal population of the low-lying d−d state from the ^{3}MLCT state, resulting in radiationless decay to the ground state. Apparently, the effect of the CNx ligand compared to that of a

(43) Sullivan, B. P.; Baumann, J. A.; Meyer, T. J.; Salmon, D. J.; Lehmann, H.; Ludi, A. *J. Am. Chem. Soc.* **1977**, *99*, 7368.
(44) Zhou, M.; Andrews, L.; Bauschlicher, C. W., Jr. *Chem. Rev.* **2001**, *101*, 1931.
(45) Ollino, M.; Cherry, W. R. *Inorg. Chem.* **1985**, *24*, 1417.
(46) Elfring, W. H., Jr.; Crosby, G. A. *J. Am. Chem. Soc.* **1981**, *103*, 2683.
(47) Indelli, M. T.; Bignozzi, C. A.; Marconi, A.; Scandola, F. *J. Am. Chem. Soc.* **1988**, *110*, 7381.

third bpy ligand is to decrease the thermal activation energy (ΔE in Figure 7) required to reach the intersection region, thus greatly enhancing the MLCT → d−d transition rate.[9]

Summary

Ruthenium(II) bis-bipyridine complexes containing CNx as a ligand were synthesized and characterized. The presence of CNx was confirmed by the following data: (1) According to the X-ray study, the Ru−N bond lengths of **3** trans to the CNx ligands are considerably longer, by ∼0.03−0.04 Å, compared to the Ru−N distance cis to the isocyanide. Similarly, the DFT geometry optimization produced longer Ru−N distances for the bpy N atom trans to the isocyanide. (2) The calculated Mulliken charge on ruthenium decreases by ∼0.32 electrostatic units per CNx ligand compared to ∼0.1 units per N donor atom. (3) The HOMO and LUMO energy gaps increase from **1** to **3** as shown in Figure 5, in agreement with the blue shifts of the absorption and emission manifolds. (4) Redox potentials increase in the series from **1** to **3** in accord with the HOMO and LUMO energy changes shown in Figure 5. (5) The complexes are highly emissive at 77 K but are nonemissive at room temperature. (6) The emission lifetimes of the complexes increase from ∼3 μs for **1** to 25 μs for **3** at 77 K, in accord with the increase of the energy gap between the emitting ^{3}MLCT state and the ground state. (7) Emission curve-fitting analysis was consistent with the contribution of a ring-breathing mode near 1500 cm^{-1} in facilitating decay from the ^{3}MLCT state. (8) The C≡N stretching frequencies were computed and observed to shift to higher frequencies upon addition of the second isocyanide ligand. (9) DFT results revealed that the HOMOs contain both metal and ligand (CNx or chloro) character, whereas the LUMOs are located on the bpy ligands. Consequently, the lowest-lying singlet excited states should be labeled as MLLCT. (10) Calculations using the ^{3}MLCT geometry reveal d−d states located ∼2200−4800 cm^{-1} above it.

Acknowledgment. We acknowledge the support of Kansas NSF Cooperative Agreement EPS 987432, the Wichita State University High Performance Computing Center, the Wichita State University Office of Research Administration, the Department of Energy, The National Science Foundation, the Watkins Foundation (L.L.L.), and Parker Fellowships (J.M.V. and S.R.S.). We also thank Michael Van Stipdonk's group for the mass spectral analyses.

Supporting Information Available: Crystallographic data for complex **3** in CIF format, optimized geometries (Table S1), calculated singlet excited-state energies of **1**−**3** in ethanol (Table S2), and percent molecular orbital contributions of **1**−**3** (Table S3) in text format. This material is available free of charge via the Internet at http://pubs.acs.org.

IC049099R